Structural and Electrochemical Consequences of Sodium in the Transition-Metal Layer of O′3-Na$_3$Ni$_{1.5}$TeO$_6$

Nicholas S. Grundish,* Ieuan D. Seymour, Yutao Li, Jean-Baptiste Sand, Graeme Henkelman, Claude Delmas, and John B. Goodenough*

ACCESS | Metrics & More | Article Recommendations | Supporting Information

ABSTRACT: Sodium layered oxide cathodes for rechargeable batteries suffer from Na$^+$ ordering and transition-metal layer gliding that lead to several plateaus in their voltage profile. This characteristic hinders their competitiveness as a viable option for commercial rechargeable batteries. In O′3-layered Na$_3$Ni$_{1.5}$TeO$_6$ (Na$_{5/6}$[Na$_{1/6}$Ni$_{3/6}$Te$_{2/6}$]O$_2$), Rietveld refinement and solid-state nuclear magnetic resonance spectroscopy show that there is sodium in the transition-metal layer. This sodium within the transition-metal layer provides cation disorder that suppresses Na$^+$ ordering in the adjacent sodium layers upon electrochemical insertion/extraction of sodium. Although this material shows a reversible O′3 to P′3 phase transition, its voltage versus composition profile is typical of traditional lithium layered compounds that have found commercial success. A Ni$^{2+/3+}$ redox couple of 3.45 V versus Na$^+$/Na is observed with a specific capacity as high as 100 mAh g^{-1} on the first discharge at a C/20 rate. This material shows good retention of specific capacity, and its rate of sodium insertion/extraction can be as high as a 2C-rating with particle sizes on the order of several micrometers. The structural nuances of this material and their electrochemical implications will serve as guidelines for designing novel sodium layered oxide cathodes.
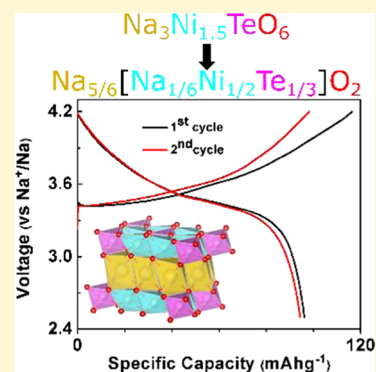
INTRODUCTION

Layered oxides have played a pivotal role in rechargeable lithium-ion (Li-ion) batteries for 40 years. The discovery of LiCoO$_2$ spurred an intense investigation into lithium compounds for rechargeable batteries.[1−10] Sodium-ion (Na ion) layered oxides were studied extensively in the 1980s,[11−13] but the commercialization of the first Li-ion battery by Sony in 1991 returned research focus to lithium-containing materials. Sodium layered oxides have now resurfaced as a growing area of interest owing to the ubiquitous accessibility of sodium and the greater degree of Na$^+$ order in layered NaMO$_2$ oxides (M = 3d transition metal). Layered sodium compounds for rechargeable battery applications are relatively easy to prepare, but suffer from major drawbacks that have prevented commercial realization of a Na-ion battery that is competitive with any of the Li-ion counterparts that have come to power everything from cell phones and large-scale power tools to hybrid electric/all-electric vehicles.

Sodium layered materials of the formula NaMO$_2$ are an alternative option for rechargeable Na-ion battery cathodes, but they are plagued by strong Na-ion ordering and ordered−ordered phase transitions brought about by the gliding of the MO$_2$ layers following sodium removal, which often results in a large volume change of the material upon cycling and an electrochemical "Devil's Staircase".[14−16] Valiant efforts have been made to prevent these structural transitions during cycling, but to date, no compound performs this task

successfully. Some layered Na-ion cathodes have high-valence cations in their transition-metal layers such as antimony (Sb^{5+}) or tellurium (Te^{6+}) that require a significant amount of divalent cations for charge compensation; for example, O′3-layered Na$_3$Ni$_2$SbO$_6$, P2-layered Na$_2$Ni$_2$TeO$_6$, and O′3-layered Na$_4$NiTeO$_6$.[17−21] Each of these materials present a honeycomb ordered structure, which can be described with the classical formula for layered oxides: Na$_x$(Ni,Na)$_{2/3}$(Sb,Te)$_{1/3}$O$_2$. The honeycomb ordering results from coulombic interactions between each Sb^{5+} or Te^{6+} ion and the neighboring Ni^{2+} and Na^{1+} ions; size difference between cations can also result in this type of ordering. The tellurium compounds in particular show a less prominent tendency towards ordered phase formation upon Na$^+$ deintercalation judging from the plateau characteristics in their voltage versus composition profiles.

In the Na$_4$NiTeO$_6$ phase, the transition-metal slab exhibits the (Na$_{1/3}$Ni$_{1/3}$Te$_{1/3}$)O$_2$ formula.[21] In an attempt to form vacancies in this structure, we settled on the stoichiometry Na$_3$Ni$_{1.5}$TeO$_6$. Our purpose was to determine whether

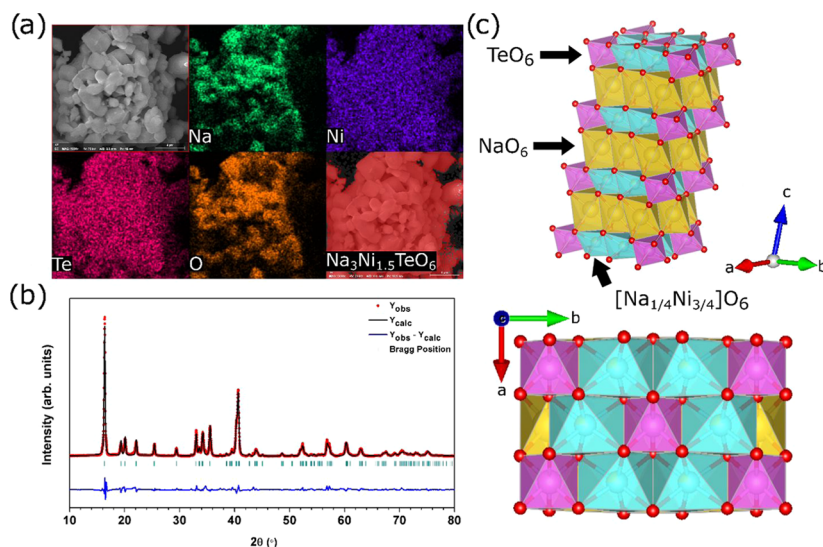**Figure 1.** (a) Scanning electron microscopy and energy-dispersive X-ray spectroscopy mapping of $Na_3Ni_{1.5}TeO_6$ particle agglomeration, highlighting the even distribution of sodium (green), nickel (purple), tellurium (magenta), and oxygen (orange) as well as phase mapping showing the agglomerate to be composed of a single-phase material. (b) Rietveld refined powder X-ray diffraction pattern of $Na_3Ni_{1.5}TeO_6$. The X-ray diffraction pattern was collected from $2\theta = 10$ to $100°$ with the $10-80°$ 2θ region shown to demonstrate the refinement quality. (c) Obtained O′3-layered structure with $C2/m$ space group; NaO_6 octahedra in the sodium layer are represented in yellow, $[Na_{1/4}Ni_{3/4}]O_6$ octahedra in the transition-metal layer are represented in cyan, and TeO_6 octahedra in the transition-metal layer are represented in light purple.

vacancies form in the sodium layer or in the MO_2 slab. We show that the Na^+ ions occupy the remaining 1/6 M-sites in the MO_2 layer that are not occupied by tellurium or nickel, forming a "sodium excess"-like compound without the presence of a 4d or 5d transition metal, which is usually a requirement to form a layered sodium excess-type material, such as Na_2RuO_3.[22-25] The presence of Te^{6+} in the MO_2 slabs requires the introduction of low-valence cations (like Ni^{2+}), which are the active ions in the redox process. $Na_3Ni_{1.5}TeO_6$ demonstrates a voltage curve typical of traditional layered Li-ion cathodes during electrochemical cycling. Upon further investigation, it was found that a reversible transition-metal layer gliding occurs providing an O′3-to-P′3 phase transition. However, the P′3 phase has a reduced unit cell primarily owing to a shorter b-axis arising from a cooperative Jahn−Teller distortion when a sufficient amount of Ni^{3+} forms upon oxidation of the material. The insights gained from relating the structural peculiarities of this material to its electrochemical performance may serve as a guide in designing new layered sodium positive electrode materials toward eventually enabling a commercially viable sodium-ion battery.

EXPERIMENTAL SECTION

Materials and Methods. $Na_3Ni_{1.5}TeO_6$ was prepared by a traditional solid-state synthesis route. Na_2CO_3 (99.8%, Acros Organics), NiO (99%, Alfa Aesar), and TeO_2 (99.99%, Alfa Aesar) were used as starting materials. A 5 wt % excess of sodium was added to combat sodium volatilization at higher temperatures. The precursors were ground in a mortar and pestle in stoichiometric amounts and pressed into pellets before being fired at 900 °C for 24 h with an intermittent grinding and repelletization after the first 12 h. The pellets were then reground, pelletized, and covered with similar powder before being fired at 1000 °C for 12 h to obtain the final O′3-layered $Na_3Ni_{1.5}TeO_6$. Heating and cooling rates of 10 °C/min were used for all furnace firings. All thermal treatments were performed in air.

X-ray Diffraction and Rietveld Refinement. X-ray diffraction was performed with a Rigaku Miniflex 600 (Cu Kα radiation) in stepping mode from 2θ of 10 to 100° with a step size of 0.02° with a 2

s time count at each step. The sample was spun during data acquisition to include as many particles with as many grain orientations as possible within the diffraction geometry. A structural model for O′3-layered $Na_3Ni_{1.5}TeO_6$ was developed from observation of the $Na_3Ni_2SbO_6$ and Li_4NiTeO_6 structures.[17,26] Once a structural model was developed, Rietveld refinement of the X-ray diffraction pattern was performed with the FullProf Suite software package. All structural images in this work were developed using the VESTA 3D structure visualization program.[27]

Exploration of the structural transformation that occurs upon cycling in O′3-layered $Na_3Ni_{1.5}TeO_6$ was done with in operando galvanostatic cycling X-ray diffraction on a Bruker D8 ADVANCE diffractometer. X-ray diffraction patterns from $2\theta = 10$ to $40°$ were taken in series with each pattern having a duration of 5 min and no intermittent time between scans. The cell was galvanostatically cycled at a C/10 rate while the diffraction patterns were being obtained.

X-ray diffraction of the ex situ samples was performed with a Panalytical Empyrean diffractometer having a Cu Kα source and an X'Celerator detector. The samples were scanned in the 2θ range of $10-80°$ at a scan rate of 0.083°/min. Le Bail fitting of the P′3 phase ex situ diffraction pattern was also performed with the FullProf Suite software package.

Scanning Electron Microscopy and Elemental Analysis. Scanning electron microscopy (SEM) on the as-prepared $Na_3Ni_{1.5}TeO_6$ powder was performed at an accelerating voltage of 20 kV with an FEI Quanta 650 ESEM. Energy-dispersive X-ray spectroscopy and phase mapping of the pristine powder were enabled by a Bruker EDX system attached on the electron microscope.

Solid-State Nuclear Magnetic Resonance Spectroscopy. ^{23}Na solid-state NMR spectra were acquired on a 400 MHz Bruker Avance III HD spectrometer with a Bruker 4 mm HXY probe at a magic angle spinning (MAS) frequency of 13 kHz. A rotor-synchronized Hahn-echo pulse sequence was used to acquire an initial spectrum with a π/2 pulse length of 2.2 μs optimized on solid NaCl at a power of 80 W. NaCl was used as a secondary shift reference at 7.21 ppm (relative to 1 M NaCl(aq)). To improve the resolution of the spectrum and obtain isotropic resonances in the absence of spinning sidebands, the pj-MATPASS sequence was used with 32 slices in the F2 dimension and 400 scans per slice.[28] All NMR measurements in this work were obtained with a recycle delay of 0.5 s.

Electrode Preparation. Electrodes for coin-cell assembly were prepared by grinding 70 wt % $Na_3Ni_{1.5}TeO_6$ active material, 25 wt % Denka black, and 5 wt % poly(tetrafluoroethylene) (PTFE) in a mortar and pestle. The active material and Denka black were first mixed until a homogeneous mixture was formed before adding in the PTFE. Once the PTFE was added, the mixture was ground again until a homogeneous electrode with dough-like consistency was obtained. The dough-like electrode mixture was then cold-rolled to form a thin free-standing electrode composite sheet.

Coin-Cell Assembly and Electrochemical Cell Testing. Coin cells with a 2032 cell architecture were assembled with $Na_3Ni_{1.5}TeO_6$ composite cathodes against a sodium-metal anode. The cells were constructed with 1 M $NaClO_4$ (99%, Alfa Aesar) in 90% propylene carbonate (99%, Aldrich) with 10% fluoroethylene carbonate (>99%, Aldrich) as the electrolyte (PC/FEC, 9:1, v/v) and Whatman glass fiber as the separator. Owing to the nature of the coin-cell components, the coin-cell samples were prepared in an Ar-filled glovebox (MBraun) with H_2O and O_2 levels below 0.1 ppm. The assembled coin-cell samples were galvanostatically cycled in the voltage range of 2.5−4.2 V versus Na^+/Na at various C-ratings noted in the manuscript. All galvanostatic cycling experiments were performed with a LANHE battery cycler. Two-electrode cyclic voltammetry on a $Na_3Ni_{1.5}TeO_6$ composite cathode against a sodium-metal anode cell was performed with an Autolab (PGSTAT 204). The cell was scanned at a rate of 1 mV/s to an upper vertex potential of 4.2 V versus Na^+/Na and a lower vertex potential of 2.5 V versus Na^+/Na. Electrode samples for the ex situ X-ray diffraction shown in Figure 6 were prepared with 80 wt % $Na_3Ni_{1.5}TeO_6$ active material, 15 wt % Denka black, and 5 wt % poly(tetrafluoroethylene) (PTFE). These ex situ electrode samples were prepared in Swagelok-type cells with sodium metal as the anode, Whatmann glass fiber separator, and 1 M $NaPF_6$ EC/DMC (1:1) + 5% FEC as the electrolyte. The Swagelok cells were cycled with a BioLogic MPG2 tester. The cells were allowed to cycle at a constant C/20 rate until the terminal voltage was reached, at which point the cell was held at that voltage until the current of the cell fell to zero to ensure all possible sodium ions were removed or reinserted into the active material at the respective voltages. Prior to taking the ex situ X-ray diffraction patterns, each sample was washed with DMC and allowed to dry to remove any residual $NaPF_6$ salt from the composite.

RESULTS AND DISCUSSION

Synthesis and X-ray Diffraction Characterization. $Na_3Ni_{1.5}TeO_6$ was synthesized via a traditional solid-state reaction from Na_2CO_3, NiO, and TeO_2 at 1000 °C in air. The synthesized $Na_3Ni_{1.5}TeO_6$ material was confirmed to be single phase with phase mapping performed with an energy-dispersive X-ray spectroscopy (EDX) system in a scanning electron microscope as well as X-ray diffraction. The scanning electron microscopy (SEM) images of the as-prepared $Na_3Ni_{1.5}TeO_6$ powder are shown in Figures 1a and S1. The material forms particles on the order of 1−8 μm in size with the smaller particles showing a tendency to agglomerate, as shown in the SEM image in Figure 1a. Energy-dispersive X-ray spectroscopy mapping ensured an even distribution of the four elements that were included in the precursor materials. Once the EDX spectra (Figure S2) and elemental mapping had been performed, the particles were phase-mapped to ensure that they were of single phase. An additional elemental/phase mapping and EDX spectrum of single free-standing particles and their phase purities are given in Figures S1 and S3. The desired stoichiometry of the material was confirmed from the energy-dispersive X-ray spectrum having the ratio of cations calculated as 3.0 Na/1.45 Ni/1.08 Te.

The X-ray diffraction study shows that $Na_3Ni_{1.5}TeO_6$ crystallizes in the monoclinic system ($C2/m$ space group) with an O′3-layered stacking according to the notation set

forth by Delmas.[29] The Rietveld refined X-ray diffraction pattern is shown in Figure 1b (χ^2: 7.82, R_{Bragg}: 5.91). A structural model for refinement was developed by considering the analogous structures of Li_4NiTeO_6, $Na_3Ni_2SbO_6$, and Na_4NiTeO_6.[17,21,26] The resulting structural depiction developed from these techniques is portrayed in Figure 1c. This refinement shows the presence of Na^+ ions in the MO_2 slab and of vacancies in the Na layer, leading to the crystallographic formula $Na_{5/6}[Na_{1/6}Ni_{1/2}Te_{1/3}]O_2$. To confirm this result, a structural refinement with all of the sodium ions within the Na layer and 1/6 vacancies in the transition-metal layer was performed (Figure S4). A comparison of the two refinements shows that the transition-metal MO_2 layer does not contain any vacancies and is fully occupied. Although this ordering results in a small number of vacancies (1/6 per formula unit) in the adjacent sodium layers, it does not cause enough sodium vacancies for the formation of prismatic sites in the sodium layer when synthesized. Formation of a P2-layered structure with trigonal prismatic site coordination in the sodium layer via high-temperature synthesis is often the result when a layered sodium compound is synthesized near the composition $Na_{2/3}MO_2$.[14,29] In the $Na_3Ni_{1.5}TeO_6$ structure, Na ions occupy edge-sharing octahedral sites within the sodium layer, while the transition-metal layer displays a honeycomb ordering of TeO_6 octahedra coordinated by NiO_6 and NaO_6 octahedra. The occupied octahedral sites within the transition-metal layer are also edge-sharing. A summary of the crystallographic information of the $Na_3Ni_{1.5}TeO_6$ material is given in Table 1. The relationships between the original hexagonal cell of the

Table 1. Rietveld Refinement Results and Crystallographic Information for $Na_3Ni_{1.5}TeO_6$[a]

space group: $C2/m$, a_{mon} = 5.3251 Å, b_{mon} = 9.2034 Å, c_{mon} = 5.7320 Å, α_{mon} = γ_{mon} = 90°, β_{mon} = 108.57°, $c \sin \beta$ = 5.434 Å					
atom	coordinates			occ.	wyck.	sym.
Te	0.00000	0.00000	0.00000	1.000	2a	2/m
Ni	0.00000	0.32660	0.00000	0.75	4g	2
Na1	0.00000	0.32660	0.00000	0.25	4g	2
Na2	0.00000	0.18390	0.50000	0.833	4h	2
Na3	0.00000	0.50000	0.50000	0.833	2d	2/m
O1	0.75200	0.00000	0.22570	1.000	4i	m
O2	0.72900	0.64050	−0.82970	1.000	8j	1

R_{wp} =13.1; R_{Bragg} = 5.91; χ^2 = 7.82

[a]In the first step of the refinement, the 4g site occupancy by Ni^{2+} and Na^+ (equal to 0.747 and 0.247, respectively) was free. Their sum being close to 1 is evidence of the sodium presence in the layer. Therefore, in the final refinement, the sum was fixed to 1.

O3 structure, the O3 supercell, and the monoclinic cell in the basal plane are provided in Figure S5. The stoichiometric formula, which emphasizes the cationic distribution in the layered oxides, is therefore: $Na_{5/6}(Na_{1/6}Ni_{1/2}Te_{1/3})O_2$. This composition for the O′3 structure is quite unusual for a material obtained with high-temperature solid-state synthesis; nevertheless, it has been reported for the $Na_{0.9}CoO_2$ phase.[30]

Nuclear Magnetic Resonance Spectroscopy. Based on the indication from the powder X-ray diffraction pattern that sodium ions reside in the transition-metal layer, ^{23}Na solid-state nuclear magnetic resonance spectroscopy (NMR) was performed to elucidate the specific Na^+ ion locations within the $Na_3Ni_{1.5}TeO_6$ structure. The spectrum of $Na_3Ni_{1.5}TeO_6$ (Figure 2a) obtained with the pj-MATPASS pulse sequence

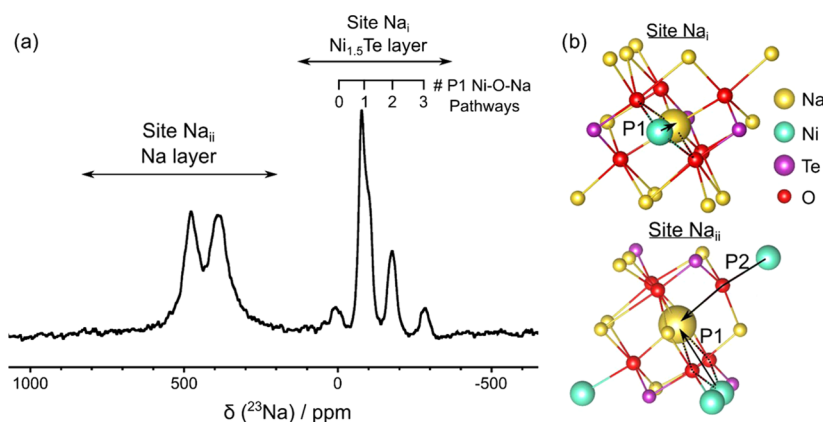**Figure 2.** (a) ^{23}Na pj-MATPASS NMR spectrum of $Na_3Ni_{1.5}TeO_6$ acquired at 400 MHz and 13 kHz MAS. The 1D pj-MATPASS spectrum in (a) shows only the pure isotropic resonances of different ^{23}Na sites, which has been obtained by shearing and summing the full 2D pj-MATPASS spectrum (Figure S6). (b) Local bonding environments of two types of Na ions in the $Na_3Ni_{1.5}TeO_6$ structure: site Na_i ($Ni_{1.5}Te$ layer) and site Na_{ii} (Na layer). Spin transfer along 90° (P1) and 180° (P2) Ni^{2+}–O–Na bond pathways is indicated with the black arrows. The total P1 pathway consists of two different 90° Ni^{2+}–O–Na bond pathways, which are indicated by the dashed lines. The ^{23}Na NMR shift regions corresponding to the two types of Na site are indicated in (a) along with the number of P1 pathways connected to different Na_i sites.

contains six isotropic Na resonances: two positively shifted peaks with maximum intensities at 386 and 477 ppm, and four negatively shifted peaks with maximum intensities at 0, −77, −178, and −283 ppm. Several of these peaks show asymmetric line shapes owing to the quadrupole nature of the ^{23}Na nucleus ($I = 3/2$). A detailed fitting of the quadrupole parameters of each environment was not attempted in this study due to the possible distortions of the line shapes as a result of the use of the pj-MATPASS sequence. However, an indication of the difference in the quadrupole parameters of the different sites can be gauged from the difference in the nutation behavior of the Hahn-echo spectra (Figure S7).

The dominant contribution to the ^{23}Na NMR shift in Figure 2a is related to the Fermi contact interaction in which unpaired spin density is transferred from Ni^{2+} ($t_{2g}^6e_g^{*2}$) to the Na nucleus via an intermediate O ligand.[20] The total ^{23}Na NMR shift observed experimentally can be decomposed into the sum of the individual contributions from each Ni^{2+}–O–Na bond pathway.[31−33] In O′3-$Na_3Ni_{1.5}TeO_6$, the Na ions in octahedral sites within the Na layer (Na_{ii}) can experience both 90° Ni^{2+}–O–Na (P1) and 180° Ni^{2+}–O–Na (P2) bond pathway contributions with Ni^{2+} in the transition-metal layer, as shown in Figure 2b. Only P1 pathways are possible for Na^+ ions occupying octahedral sites in the transition-metal layer (Na_i). For both types of sites, the number of Ni^{2+}–O–Na bond pathways connected to a particular site will depend on the ordering of Ni^{2+}, Na^+, and vacancies in the transition-metal layer.

$^{6/7}$Li NMR studies on analogous Li-cathode materials show that 90° Ni^{2+}–O–Na P1 pathways are expected to lead to small negative shift contributions, while 180° Ni^{2+}–O–Na P2 pathways are expected to result in positive shift contributions that are much larger owing to differences in the orbitals that are overlapping.[34] Therefore, the Na sites with positive shifts (386 and 477 ppm) in Figure 2a can be assigned to Na_i sites in the Na layer, which experience large positive P2 contributions. The difference in the shift of 91 ppm between the Na_{ii} sites results from the difference in the number of P1 pathways. The four sharp peaks at 0, −77, −178, and −283 ppm can then be assigned to Na_i sites in the transition-metal layer, which only experience negative P1 pathways. The separation of the negative peaks (0, −77, −178, and −283 ppm) is almost

constant at 77−105 ppm, suggesting that these environments can be assigned to Na_i sites with 0, 1, 2, or 3 Ni^{2+} neighbors, respectively, along P1 pathways, as indicated in Figure 2a. The slight difference between the P1 pathway contributions for different Na_i sites is likely due to small differences in the Ni^{2+}–O–Na bond lengths as well as differences in the second-order quadrupole shift for sites with varying quadrupole coupling constants (C_q). The distribution of the intensities of the peaks associated with Na_{ii} sites suggests that there is a preference for Na to occupy sites in the transition-metal layer with a single Ni^{2+} neighbor. The detailed analysis of Na ordering within the $Na_3Ni_{1.5}TeO_6$ structure is beyond the scope of the current study and will be the subject of future work. These findings from the NMR data definitively show that we have effectively obtained sodium in the transition-metal layer. Without Na^+ ions in the transition-metal layer, each Te^{6+} would be surrounded by 4 Ni^{2+} and two vacancies, which would lead to an unstable charge distribution in the MO_2 slab. The presence of 4 Ni^{2+} and 2 Na^+ around a Te^{6+} ion leads to the question of long-range ordering between Ni^{2+} and Na^+ in the MO_2 slabs. However, long-range ordering of 4 Ni^{2+} and 2 Na^+ around each Te^{6+} ion, which are honeycomb ordered, would require a very large unit cell. The X-ray diffraction pattern does not exhibit any extra diffraction lines that are not indexed with our structural model; therefore, this hypothesis is not considered. With a better understanding of the structure elucidated with powder X-ray diffraction and solid-state NMR as well as a confirmed single-phase pure material shown via elemental/phase mapping, we began electrochemical testing of the O′3−$Na_3Ni_{1.5}TeO_6$.

Electrochemical Behavior. The composition upon charge/discharge of $Na_xNi_{1.5}TeO_6$ was tracked with galvanostatic cycling to assess how much sodium could be removed from the material. Cells were assembled with a $Na_3Ni_{1.5}TeO_6$ composite cathode, sodium-metal anode, glass fiber separator, and 1 M $NaClO_4$ PC/FEC (9:1) electrolyte. These cells were cycled at C/10 and C/20 rates; the resulting voltage versus composition curves are presented in Figure 3. Extraction of sodium ions begins at 3.45 V versus Na^+/Na. The low overpotential between insertion/extraction of sodium as well as the voltage at which insertion/extraction occurs indicates the redox activity is primarily owing to the $Ni^{2+/3+}$ redox

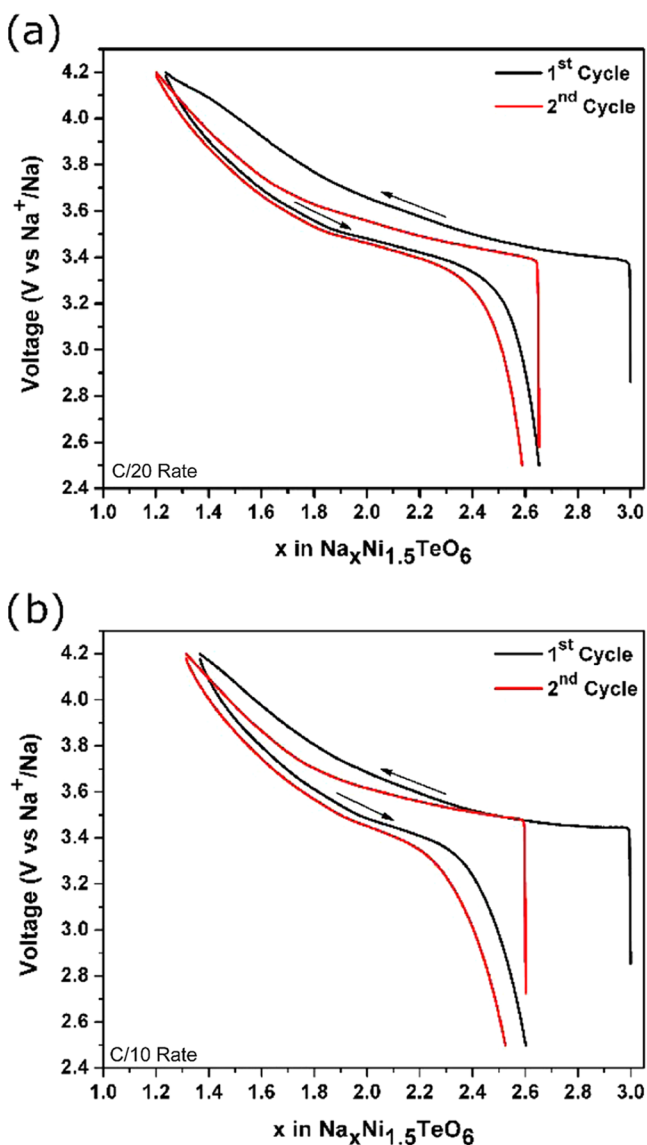**Figure 3.** Voltage versus composition curves for O′3-layered $Na_3Ni_{1.5}TeO_6$. Total sodium content within material cycled at (a) C/20 and (b) C/10 rates. Each cell was cycled against sodium metal with 1 M $NaClO_4$ PC/FEC (9:1) (v/v) as the electrolyte.

couple with a small contribution past 1.5 formula units of sodium removed to the $Ni^{3+/4+}$ redox couple. At the end of charge at 4.2 V, the composition of the final material is close to $Na_{1.2}Ni_{1.5}TeO_6$. This formula shows that, in this phase, there is $1.2Ni^{3+}$ and $0.3Ni^{4+}$. With such a small amount of Ni^{4+}, we do not expect oxygen oxidation to occur during cycling. In lithium- and sodium-rich layered materials, oxygen oxidation only occurs when all other cations are in their maximum available oxidation state. Additionally, in previous work reported on Li_4NiTeO_6, it was shown through X-ray photoelectric spectroscopy that the only redox activity upon lithium removal from the material was from the $Ni^{2+/3+}$ and $Ni^{3+/4+}$ redox couples without any evidence of anionic redox, even when the cell was taken to 5 V versus Li^+/Li.[26] The 3.45 V versus Na^+/Na of the Ni^{2+}/Ni^{3+} redox couple in this material as well as the single voltage at which sodium is removed was confirmed with cyclic voltammetry (Figure S8). A single peak manifests itself upon sodium extraction during the positive sweep. Similar materials containing tellurium have allowed for

full operation of the $Ni^{2+/3+}$ and $Ni^{3+/4+}$ redox couples; however, for these sodium compounds, the charging voltage cutoff is too high to differentiate whether Na ions are being removed or the organic−liquid electrolyte is being irreversibly oxidized. This irreversible oxidation of the electrolyte would account for the poor coulombic efficiencies that have been reported for the P2-layered $Na_2Ni_2TeO_6$ and O′3-layered Na_4NiTeO_6 compounds, but a full investigation as to the nature of Na-ion insertion/extraction of these materials has yet to be reported.[19−21] It is possible that kinetic and/or thermodynamic barriers to sodium reinsertion into these materials beyond a certain sodium content could be partially, if not fully, responsible for the poor first-cycle efficiency; this point is further discussed below. One should note the high voltage of the $Ni^{2+/3+}$ redox couple versus other layered oxides with only 3d transition metals in the slab. As an example, Ni^{2+} in P2−$Na_xMn_{0.6}Ni_{0.3}Co_{0.1}O_2$ is oxidized to Ni^{3+} in the 2.3−3.5 V range, while it occurs in the 3.45−4.0 V range in $Na_xNi_{1.5}TeO_6$.[35] The high voltage of the $Ni^{2+/3+}$ redox couple in these Te-based materials is not unusual. Previous reports on $Na_2Ni_2TeO_6$, Na_4NiTeO_6, $Li_2Ni_2TeO_6$, and Li_4NiTeO_6 have shown that the TeO_6 octahedra provide an inductive effect that lowers the energy of the $Ni^{2+/3+}$ redox couple, creating a larger potential difference with the Fermi level of the sodium.[20,21,26,36] Although the TeO_6 octahedron is not a polyanion that is normally expected to show an inductive effect, the strong Te−O covalent bonding provides a similar function on the electronic structure of the material by making the Ni−O bonding more ionic. The more ionic the Ni−O bond, the lower the energy of the antibonding e_g^* orbital of the material becomes, which is responsible for redox activity in the d^8 electron configuration of Ni^{2+}.

Specific capacity and coulombic efficiency plots along with the corresponding voltage versus specific capacity curves of galvanostatic charge/discharge cycling at C/20 and C/10 rates for the $Na_3Ni_{1.5}TeO_6$ cathode are shown in Figure 4a−d. The charging voltage profile of the material shows only a narrow single plateau followed by a sloping curve until the voltage cutoff of 4.2 V. This behavior will be discussed further with the "in operando" X-ray diffraction experiment. Similarly, the discharge voltage profile shows a sloping curve until the 3.45 V plateau is reached. The $Na_3Ni_{1.5}TeO_6$ cathode shows a slight irreversible capacity loss upon the first charge that is discussed in more detail below. A steady decrease in specific capacity is seen upon cycling at both C/20 and C/10 rates. After 50 cycles at a C/20 rate, 79% of the first discharge capacity is maintained, while after 100 cycles at a C/10 rate, 73% of the first cycle discharge capacity was retained. At a C/20 rate (Figure 4a,b), roughly 1.8 formula units of sodium are removed upon first charge with 1.45 formula units of sodium reinserted into the material on first discharge, which corresponds to a 100 mAh g^{-1} discharge specific capacity. Galvanostatic cycling at a C/10 rate (Figure 4c,d) allowed for 1.63 formula units of sodium to be extracted on first charge with 1.24 formula units reinserted on first discharge, corresponding to a specific discharge capacity of 87.3 mAh g^{-1}. A larger irreversible first cycle capacity loss for galvanostatic cycling at a C/10 rate over cycling at a C/20 rate suggests that the capacity fade is related to a kinetic barrier to sodium reinsertion into the material.

The rate capability of the $Na_3Ni_{1.5}TeO_6$ cathode is shown in Figure 4e; the corresponding voltage versus specific capacity curve for each C-rate is shown in Figure 4f. The P2-layered
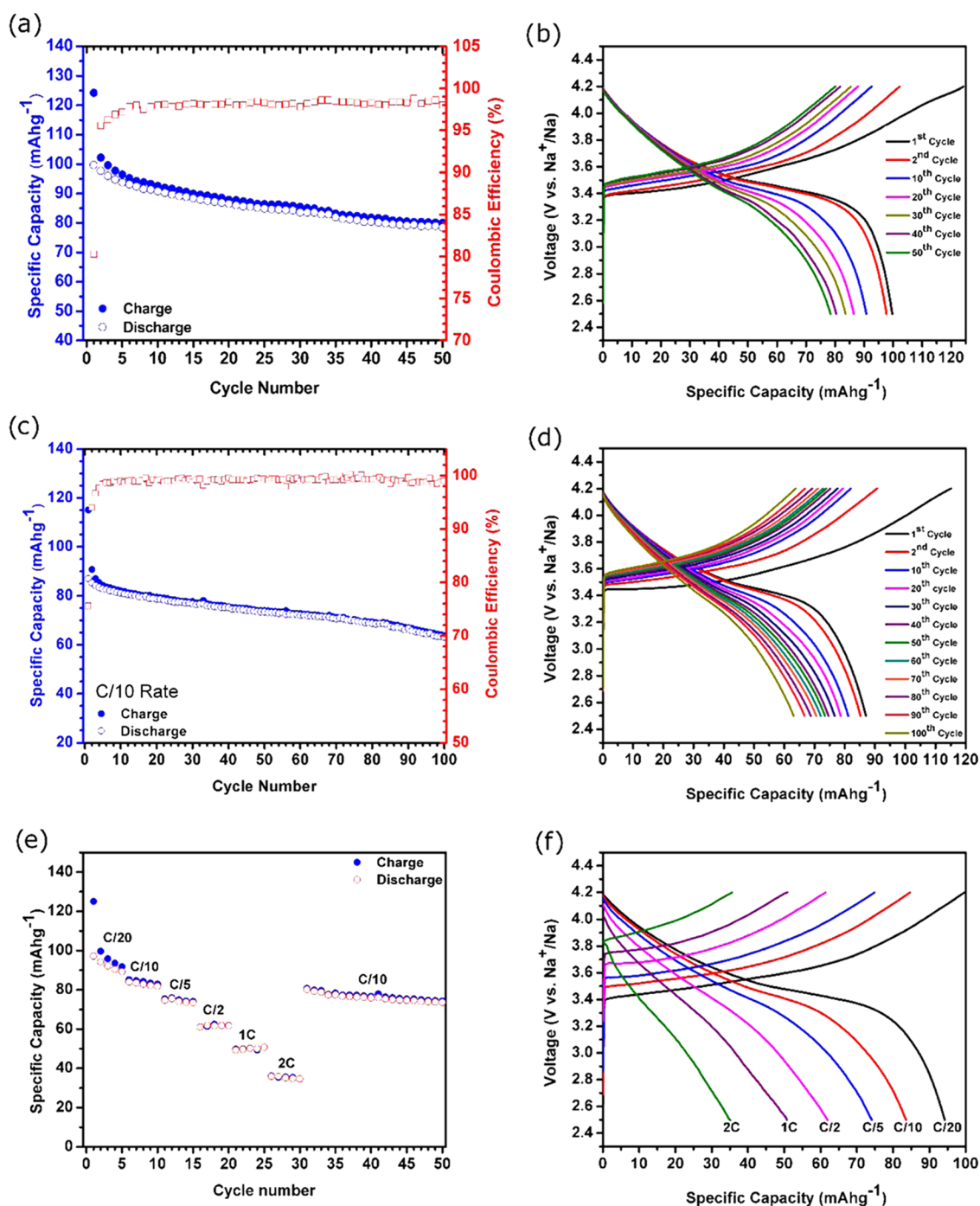
Figure 4. (a) Specific capacity and coulombic efficiency of $Na_3Ni_{1.5}TeO_6$ galvanostatically cycled at a C/20 rate against sodium metal with 1 M $NaClO_4$ PC/FEC (9:1) (v/v) as the electrolyte. (b) Corresponding voltage versus specific capacity curves for the cell shown in (a). (c) Specific capacity and coulombic efficiency of a cell with same configuration as (a), but galvanostatically cycled at a C/10 rate. (d) Corresponding voltage versus specific capacity curves for the cell shown in (c). (e) Specific capacity of a cell with the same configuration as (a), but galvanostatically cycled at varying C-rates. (f) Corresponding voltage versus specific capacity curves at each C-rating for the cell shown in (e).

$Na_2Ni_2TeO_6$ and O′3-layered Na_4NiTeO_6 compounds have previously shown multiple voltage plateaus in their charge/discharge voltage profiles, which is a tell-tale sign of sodium ordering or ordered−ordered phase transitions within the material. Thus, there is no evidence of Na-ion ordering within the sodium layer of $Na_xNi_{1.5}TeO_6$ contrary to what is frequently observed in Na-layered oxides. As previously shown, the Ni^{2+} and Na^+ ions are distributed among the 4g sites of the (Na,Ni,Te)O_2 slabs (Table 1). One can assume

that this shared site occupancy in the transition-metal layer prevents sodium ordering in the adjacent interslab space.

Phase Transformation. In operando galvanostatic X-ray diffraction was performed to explore the nature of the voltage curve of $Na_3Ni_{1.5}TeO_6$ as well as to elucidate the irreversible first-cycle capacity loss. To simplify the following discussion about the phase transition in this material, we will use the classical formula for layered oxides $(Na_{0.83}[Na_{1/6}Ni_{1/2}Te_{1/3}]$-$O_2)$. The charge/discharge curves with the two formula

descriptions relative to this in operando experiment are given in Figure S9. Selected domains of the in operando X-ray diffraction patterns for the first two cycles, showing the changes in the interslab distance, are provided in Figure 5. A
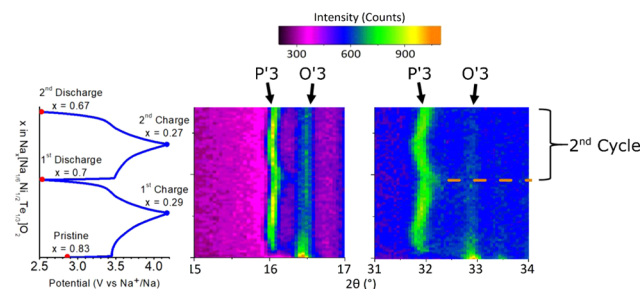

Figure 5. In operando X-ray diffraction data collected during the first two galvanostatic charge/discharge cycles of a $Na_{0.83}[Na_{1/6}Ni_{1/2}Te_{1/3}]O_2$ ($Na_3Ni_{1.5}TeO_6$) versus sodium-metal cell with 1 M $NaClO_4$ PC/FEC (9:1) (v/v) as the electrolyte showing the phase transformation from an O′3 stacking structure to a P′3 stacking of the $Na_{0.5}Ni_{1.5}TeO_2$ slabs. The change in intensity of the (003) lines (16 and 16.5°) and (006) lines (32 and 33°) indicates the structural evolution which occurs mainly in the first cycle.

sudden shift in the initial peak from the (00*l*) plane of the structure begins almost immediately as sodium is removed from the material. Once 0.03 Na^+ ions are deintercalated from $Na_{0.83}[Na_{1/6}Ni_{1/2}Te_{1/3}]O_2$, a secondary peak with a much higher *d*-spacing (lower 2θ) appears with the formation of a new phase. The peak representing the initial O′3-layered structure became nonexistent after 0.06 sodium per formula unit had been deintercalated from the structure. This shift can be attributed to the formation of a new layered $Na_{0.77}[Na_{1/6}Ni_{1/2}Te_{1/3}]O_2$ phase. Once this layered phase is formed, the in operando diffraction simply shows a solid solution as sodium continues to be removed and reinserted into the material upon charge and discharge. This behavior is

characteristic of the formation of P3-type oxygen packing (AB BC CA) by slab gliding from O3 oxygen packing (AB CA BC), which is commonly observed for Na_xMO_2 systems.[37] The potential plateau observed at the beginning of the charge process for the first cycle can be attributed to the two-phase equilibrium between the O′3 and P′3 phases. Once the O′3 phase has fully transformed to the P′3 phase, the voltage curve begins to slope upward. At the end of the first discharge, the amount of sodium in the Na layer ($Na_{0.70}[Na_{1/6}Ni_{1/2}Te_{1/3}]O_2$) is too low to allow for the reformation of the O′3 phase. We have not considered the Na^+ ions present in the $[Na_{1/6}Ni_{1/2}Te_{1/3}]O_2$ slab to be involved in the deintercalation process; this point will be addressed later on in the discussion.

To obtain higher-quality X-ray diffraction patterns that could be properly indexed, we opted to carefully prepare samples for ex situ galvanostatic X-ray diffraction, as shown in Figure 6. X-ray diffraction patterns are presented for a pristine electrode (P), an electrode charged to 4.2 V versus Na^+/Na (C), and an electrode charged to 4.2 V then discharged to 2.5 V versus Na^+/Na (D). The sample charged to 4.2 V as well as the sample charged to 4.2 V and discharged to 2.5 V were held at the terminal voltage of the experiment until the current of the cell fell to zero; the Na content in the sodium layer of these materials when taken for X-ray diffraction corresponds to $Na_{0.21}$ and $Na_{0.78}$, respectively. At this point, the composite electrodes were removed and washed prior to obtaining X-ray diffraction patterns. The diffraction pattern of the pristine material shows all of the peaks of the original layered $Na_{0.83}[Na_{1/6}Ni_{1/2}Te_{1/3}]O_2$ ($Na_3Ni_{1.5}TeO_6$) material as well as a few additional peaks that can be attributed to the carbon black/graphite mixture and binder that were used in the preparation of the electrode. Several diffraction peaks (particularly those related to the superstructure) have less intensity than expected in the ex situ diffraction patterns. This behavior is characteristic of preferential orientation, which occurs when the active material is ground with the carbon and PTFE during electrode preparation. The X-ray diffraction
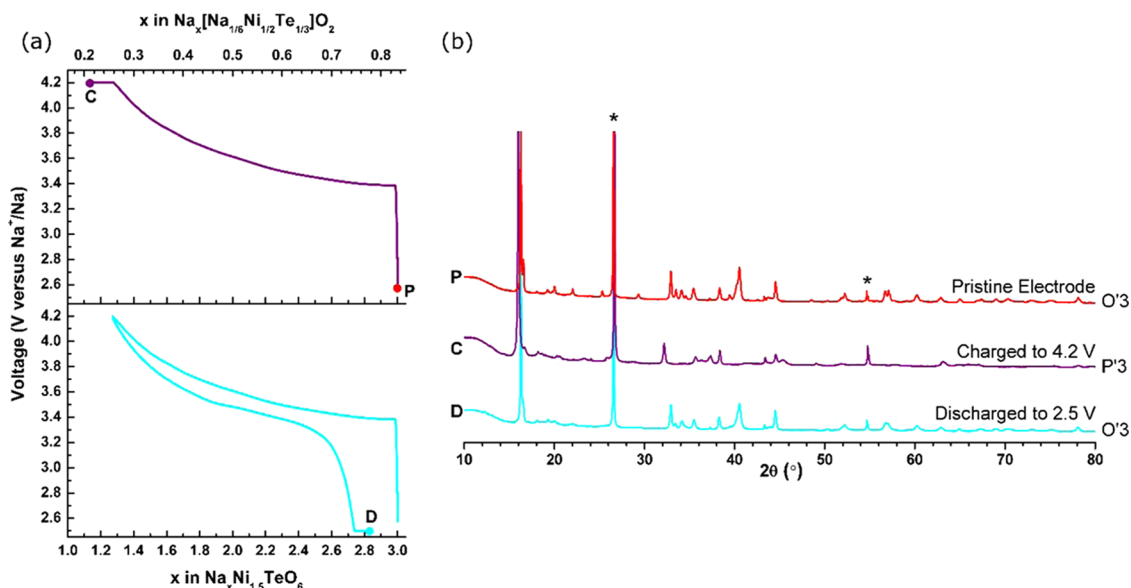

Figure 6. Ex situ X-ray diffraction patterns and corresponding voltage versus composition curve. The sample charged to 4.2 V and the sample charged to 4.2 V and discharged to 2.5 V were galvanostatically cycled against a sodium-metal anode with 1 M $NaPF_6$ EC/DMC (1:1) + 5% FEC as the electrolyte. Each sample was held at the terminal voltage until the current of the cell fell to zero. * designates peaks from conductive carbon additive or other electrode composite components within the electrode.

pattern of the electrode that was extracted after being charged to 4.2 V versus Na^+/Na shows a significant change in intensity of some of the diffraction lines, while after discharge, the pattern is very similar to that of the pristine electrode. This result shows the reversibility of the electrochemical reaction and suggests that the potentiostatic hold at 2.5 V versus Na^+/Na is an important factor driving the phase transformation back to the O′3 phase. With no additional capacity below the 2.5 V lower voltage limit as indicated by the sharp decline of the voltage curve after the primary redox activity above 3.2 V, the barrier to reforming the O′3 phase is primarily kinetic. Thus, it becomes difficult for Na ions to insert into the material with increasing Na concentration in the cathode upon discharge. Once a thin layer of the O′3 phase is formed around the large P′3 particles (sub 1 μm) during discharge, the tetrahedral sites that bridge adjacent octahedral sites within the sodium layer of the O′3 phase form a diffusion bottleneck for Na^+ ions decreasing ionic conductivity from that of the P′3 phase where Na^+ ions can move with relative ease between the face-sharing trigonal prismatic sites. As soon as the O′3 phase starts to form on the particle surface, the Na^+ concentration increases rapidly on the outermost surface, leading to a small number of vacancies and poorer ionic diffusivity. These considerations explain the large first-cycle capacity loss in this material in the half-cell configurations when no potentiostatic hold is present in the galvanostatic cycling experiments.

The diffraction patterns of P3- and O3-type materials have distinct characteristics that allow their unambiguous determination. Most notably, there is a change in the relative intensity of the peaks related to the (104) and (105) planes when the diffraction pattern is indexed to the small hexagonal cell ($R\bar{3}m$ space group). When the ratios of intensities of the (104) and (105) peaks are such that the $I_{(104)}/I_{(105)}$ ratio is large, the structure displays O3-type packing. However, a small $I_{(104)}/I_{(105)}$ ratio is characteristic of P3-type packing.[15] A comparison of the ex situ diffraction patterns in the $(104)_{hex}$ and $(015)_{hex}$ peak regions of the $R\bar{3}m$ space group is provided in Figure S10. The pristine electrode shows a large intensity in the $(104)_{hex}$ peak domain, but weak intensity in the $(015)_{hex}$ domain. This result is consistent with the powder diffraction pattern of the as-prepared material, showing an O′3-layer stacking. However, upon charging to 4.2 V, there is a change in the relative intensities of the $(104)_{hex}$ and $(105)_{hex}$ peaks domains, giving a much smaller $I_{(104)}/I_{(105)}$ ratio. Thus, at full charge to 4.2 V versus Na^+/Na, the material shows P3 stacking. This diffraction pattern was fitted with the Le Bail method to obtain unit-cell parameters and to check for distortion to a monoclinic symmetry (Figure S11). The material maintained the $C2/m$ space group, giving it the P′3-layered structure designation. Table 2 gives the monoclinic unit-cell parameters

Table 2. Monoclinic Unit Cell Parameters of P′3– $Na_{1.2}Ni_{1.5}TeO_6$ Obtained from Le Bail Fitting of the Ex Situ XRD Pattern

space group	$C2/m$
a	5.082 Å
b	8.627 Å
c	5.682 Å
β	104.8°
$c \sin \beta$	5.494 Å

of the P′3 phase obtained with a Le Bail fit. These lattice parameters can be compared with those of the O′3 pristine material (Table 1). The decrease in the a and b parameters results from the in-plane cell contraction due to nickel oxidation. The octahedral-to-prismatic change as well as the decrease in the Na content of the material, which leads to a smaller lattice cohesion, results in an increase in $c \sin \beta$. In layered materials, the Jahn−Teller distortion of the MO_6 octahedra (Mn^{3+} or Ni^{3+}) leads to a departure of the $a_{mon.}/b_{mon.}$ ratio from the ideal $\sqrt{3}$ value (1.87 for $NaNiO_2$).[33] The relation between the various cells is shown in Figure 7. In the case of the superstructure cell resulting from the honeycomb ordering, the distortion is characterized by the $3a_{mon.}/b_{mon.}$ ratio, which is equal to 1.78 for the deintercalated P′3 versus 1.74 for the pristine O′3 phase. This increase of the $3a_{mon.}/b_{mon}$ results from a cooperative Jahn−Teller distortion triggered by the transition from Ni^{2+} to predominantly Ni^{3+} with a small amount of Ni^{4+} in the material after being charged to 4.2 V coupled with the honeycomb ordering of the transition-metal layer. The presence of a significant amount of inactive Jahn−Teller ions (Te, Na) makes a full cooperative distortion difficult, leading to a smaller departure from the $3a_{mon}/b_{mon}$ ratio (1.78) for the P′3 phase versus the a/b ratio (1.87) for $NaNiO_2$.[33]

In discussing the O′3 and P′3 phase transition, we assumed that the Na^+ ions present in the $[Na_{1/6}Ni_{1/2}Te_{1/3}]O_2$ layer are not involved in the deintercalation process but do contribute to a better charge distribution in this layer for the pristine material. Generally, the transition in layered materials from O3 to P3 stacking occurs when the Na^+ ions are deintercalated only from the sodium layer. In this case, if the sodium ions present in the $[Na_{1/6}Ni_{1/2}Te_{1/3}]O_2$ layer were deintercalated upon charge, the amount of Na^+ ions in the sodium layer would remain almost constant over the range of $0 \leq x \leq 1/6$ in $Na_{5/6}[Na_{1/6}Ni_{1/2}Te_{1/3}]O_2$ during charge and the O3-type structure would be maintained during this time for some time upon cell charging. Thus, the rapid occurrence of the O3 to P3 transition on removing only $Na_{0.06}$ from the material is evidence that the sodium in the transition-metal layer is not involved in the initial deintercalation process.

■ CONCLUSIONS

O′3-layered $Na_3Ni_{1.5}TeO_6$ displays some unusual phenomena that will prove useful when considering new cathode compositions for Na-ion batteries in the future. Vacancies in the sodium layer assist in a quick gliding of the transition-metal slabs when the material is charged to shift the O′3-layer stacking to a P′3-layer stacking. However, there is no evidence of further phase transitions when the material is charged up to 4.2 V versus Na^+/Na. The presence of a significant amount of Ni^{3+} increases the in-plane distortion (cooperative Jahn−Teller effect) at full charge. Although the Te^{6+} ions are fully ordered within the transition-metal layer, the sodium within this layer provides enough cation disorder to suppress Na ordering in the adjacent alkali-ion layers giving a favorable effect on the charge/discharge voltage profile of the material when cycled between 2.5 and 4.2 V versus Na^+/Na. Upon cycling, only the P′3 phase is easily formed and is primarily involved in the Na insertion/extraction process, which minimizes constraints and limits capacity fading upon continuous cycling, but has a considerable effect on the first-cycle capacity loss. Large particle size and low Na^+-ion conductivity through octahedral sites via adjacent tetrahedral sites make a kinetic barrier to
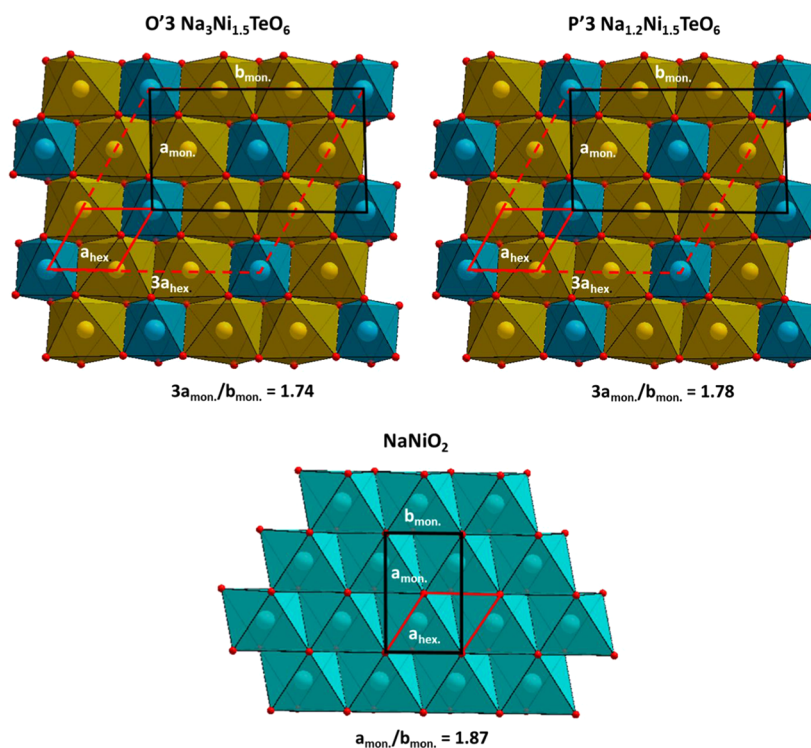
Figure 7. Jahn−Teller distortion characterized by the ratio from the in-plane cell parameters in the monoclinic system.

reforming the O′3 phase from the P′3 phase upon reinserting sodium back into the material; a potentiostatic hold at a voltage lower than the $Ni^{2+/3+}$ redox couple is necessary to fully reform the O′3 − $Na_{3-x}Ni_{1.5}TeO_6$ material.

■ ASSOCIATED CONTENT

Ⓢ Supporting Information

The Supporting Information is available free of charge at https://pubs.acs.org/doi/10.1021/acs.chemmater.0c03248.

> EDS spectra of the pristine $Na_3Ni_{1.5}TeO_6$ material; Rietveld refinement of the $Na_3Ni_{1.5}TeO_6$ structure assuming all sodium resides within the sodium layer and a corresponding table of crystallographic parameters obtained from this refinement; schematic of the relation between the O3 hexagonal unit cell and the monoclinic unit cell of the honeycomb ordered $Na_3Ni_{1.5}TeO_6$ structure; 2D pj-MATPASS and Hahn echo NMR spectra of pristine $Na_3Ni_{1.5}TeO_6$ powder; cyclic voltammogram and voltage−composition curves of $Na_3Ni_{1.5}TeO_6$ comparing the total sodium content in the material against the sodium content within the sodium layer; further comparison and analysis of the ex situ X-ray diffraction patterns presented in Figure 6; and Le Bail fit of the ex situ X-ray diffraction pattern of the P′3 phase at full charge (PDF)

■ AUTHOR INFORMATION

Corresponding Authors

Nicholas S. Grundish − *Materials Science and Engineering Program and Texas Materials Institute, The University of Texas at Austin, Austin, Texas 78712, United States;* ⓘ orcid.org/0000-0003-1821-6734; Email: nicholas.grundish@utexas.edu

John B. Goodenough − *Materials Science and Engineering Program and Texas Materials Institute, The University of Texas at Austin, Austin, Texas 78712, United States;* ⓘ orcid.org/0000-0001-9350-3034; Email: jgoodenough@mail.utexas.edu

Authors

Ieuan D. Seymour − *Department of Chemistry and the Oden Institute for Computational Engineering and Sciences, The University of Texas at Austin, Austin, Texas 78712, United States*

Yutao Li − *Materials Science and Engineering Program and Texas Materials Institute, The University of Texas at Austin, Austin, Texas 78712, United States;* ⓘ orcid.org/0000-0003-0798-6880

Jean-Baptiste Sand − *ICMCB, CNRS, Universite' de Bordeaux, Bordeaux INP, 33600 Pessac, France*

Graeme Henkelman − *Department of Chemistry and the Oden Institute for Computational Engineering and Sciences, The University of Texas at Austin, Austin, Texas 78712, United States;* ⓘ orcid.org/0000-0002-0336-7153

Claude Delmas − *ICMCB, CNRS, Universite' de Bordeaux, Bordeaux INP, 33600 Pessac, France*

Complete contact information is available at:
https://pubs.acs.org/10.1021/acs.chemmater.0c03248

Notes

The authors declare no competing financial interest.

■ ACKNOWLEDGMENTS

■ REFERENCES

(1) Mizushima, K.; Jones, P. C.; Wiseman, P. J.; Goodenough, J. B. Li_xCoO_2 (0<x<−1): A New Cathode Material for Batteries of High Energy Density. *Mater. Res. Bull.* **1980**, *15*, 783−789.

(2) Thackeray, M. M.; Johnson, P. J.; de Picciotto, L. A.; Bruce, P. G.; Goodenough, J. B. Electrochemical Extraction of Lithium from $LiMn_2O_4$. *Mater. Res. Bull.* **1984**, *19*, 179−187.

(3) Liu, W.; Kowal, K.; Farrington, G. C. Mechanism of the Electrochemical Insertion of Lithium into $LiMn_2O_4$ Spinels. *J. Electrochem. Soc.* **1998**, *145*, 459−465.

(4) Padhi, A. K.; Nanjundaswamy, K. S.; Goodenough, J. B. Phospho-olivines as Positive-Electrode Materials for Rechargeable Lithium Batteries. *J. Electrochem. Soc.* **1997**, *144*, 1188−1194.

(5) Ferg, E.; Gummow, R. J.; Kock, A. de.; Thackeray, M. M. Spinel Anodes for Lithium-Ion Batteries. *J. Electrochem. Soc.* **1994**, *141*, L147−L150.

(6) Carlier, D.; Croguennec, L.; Ceder, G.; Ménétrier, M.; Shao-Horn, Y.; Delmas, C. Structural Study of the $T^{\#}2\text{-}Li_xCoO_2$ (0.52 <x ≤ 0.72) Phase. *Inorg. Chem.* **2004**, *43*, 914−922.

(7) Tournadre, F.; Croguennec, L.; Saadoune, I.; Weill, F.; Shao-Horn, Y.; Willmann, P.; Delmas, C. The $T^{\#}2\text{-}Li_{2/3}Co_{2/3}Mn_{1/3}O_2$ System. 1. Its Structural Characterization. *Chem. Mater.* **2004**, *16*, 1411−1417.

(8) Tournadre, F.; Croguennec, L.; Saadoune, I.; Morcrette, M.; Willmann, P.; Delmas, C. The $T^{\#}2\text{-}Li_{2/3}Co_{2/3}Mn_{1/3}O_2$ System. 2. Its Electrochemical Behavior. *Chem. Mater.* **2004**, *16*, 1418−1426.

(9) Carlier, D.; Van der Ven, A.; Delmas, C.; Ceder, G. First-Principles Investigation of Phase Stability in the $O2\text{-}LiCoO_2$ System. *Chem. Mater.* **2003**, *15*, 2651−2660.

(10) Nadiri, A.; Delmas, C.; Salmon, R.; Hagenmuller, P. Chemical and Electrochemical Alkali Metal Intercalation in the 3D-Framework of $Fe_2(MoO_4)_3$. *Rev. Chim. Miner.* **1984**, *21*, 537−544.

(11) Braconnier, J.-J.; Delmas, C.; Fouassier, C.; Hagenmuller, P. Comportement electrochimique des phases Na_xCoO_2. *Mater. Res. Bull.* **1980**, *15*, 1797−1804.

(12) Maazaz, A.; Delmas, C.; Hagenmuller, P. A Study of the Na_xTiO_2 System by Electrochemical Deintercalation. *J. Inclusion Phenom.* **1983**, *1*, 45−51.

(13) Delmas, C.; Cherkaoui, F.; Nadiri, A.; Hagenmuller, P. A Nasicon-Type Phase as Intercalation Electrode: $NaTi_2(PO_4)_3$. *Mater. Res. Bull.* **1987**, *22*, 631−639.

(14) Delmas, C. Sodium and Sodium-Ion Batteries: 50 Years of Research. *Adv. Energy Mater.* **2018**, *8*, No. 1703137.

(15) Vitoux, L.; Guignard, M.; Suchomel, M. R.; Pramudita, J. C.; Sharma, N.; Delmas, C. The Na_xMoO_2 Phase Diagram (1/2 ≤ x <1): An Electrochemical Devil's Staircase. *Chem. Mater.* **2017**, *29*, 7243−7254.

(16) Mortemard de Boisse, B.; Carlier, D.; Guignard, M.; Guerin, E.; Duttine, M.; Wattiaux, A.; Delmas, C. Influence of Mn/Fe Ratio on Electrochemical and Structural Properties of $P2\text{-}Na_xMn_{1−y}Fe_yO_2$ Phases as Positive Electrode Material for Na-Ion Batteries. *Chem. Mater.* **2018**, *30*, 7672−7681.

(17) Yuan, D.; Liang, X.; Wu, L.; Cao, Y.; Ai, X.; Feng, J.; Yang, H. A Honeycomb-Layered $Na_3Ni_2SbO_6$: A High-Rate and Cycle-Stable Cathode for Sodium-Ion Batteries. *Adv. Mater.* **2014**, *26*, 6301−6306.

(18) Kee, Y.; Dimov, N.; Staykov, A.; Okada, S. Insight into Mg-Doping Effects on $Na_3Ni_2SbO_6$ Cathode Host for Na-Ion Batteries. *Mater. Lett.* **2016**, *183*, 187−190.

(19) Evstigneeva, M. A.; Nalbandyan, V. B.; Petrenko, A. A.; Medvedev, B. S.; Kataev, A. A. A New Family of Fast Sodium Ion Conductors: $Na_2M_2TeO_6$ (M = Ni, Co, Zn, Mg). *Chem. Mater.* **2011**, *23*, 1174−1181.

(20) Gupta, A.; Buddie Mullins, C.; Goodenough, J. B. $Na_2Ni_2TeO_6$: Evaluation as a Cathode for Sodium Battery. *J. Power Sources* **2013**, *243*, 817−821.

(21) Yang, Z.; Jiang, Y.; Deng, L.; Wang, T.; Chen, S.; Huang, Y. A High-Voltage Honeycomb-Layered Na_4NiTeO_6 as Cathode Material for Na-Ion Batteries. *J. Power Sources* **2017**, *360*, 319−323.

(22) Tamaru, M.; Wang, X.; Okubo, M.; Yamada, A. Layered Na_2RuO_3 as a Cathode Material for Na-Ion Batteries. *Electrochem. Commun.* **2013**, *33*, 23−26.

(23) Rozier, P.; Sathiya, M.; Paulraj, A.-R.; Foix, D.; Desaunay, T.; Taberna, P.-L.; Simon, P.; Tarascon, J.-M. Anionic Redox Chemistry in Na-Rich $Na_2Ru_{1−y}Sn_yO_3$ Positive Electrode Material for Na-Ion Batteries. *Electrochem. Commun.* **2015**, *53*, 29−32.

(24) Zhang, X.; Qiao, Y.; Guo, S.; Jiang, K.; Xu, S.; Xu, H.; Wang, P.; He, P.; Zhou, H. Manganese-Based Na-Rich Materials Boost Anionic Redox in High-Performance Layered Cathodes for Sodium-Ion Batteries. *Adv. Mater.* **2019**, *31*, No. 1807770.

(25) Assadi, M. H. N.; Okubo, M.; Yamada, A.; Tateyama, Y. Oxygen Redox in Hexagonal Layered Na_xTMO_3 (TM = 4d Elements) for High Capacity Na Ion Batteries. *J. Mater. Chem. A* **2018**, *6*, 3747−3753.

(26) Sathiya, M.; Ramesha, K.; Rousse, G.; Foix, D.; Gonbeau, D.; Guruprakash, K.; Prakash, A. S.; Doublet, M. L.; Tarascon, J.-M. Li_4NiTeO_6 as a Positive Electrode for Li-Ion Batteries. *Chem. Commun.* **2013**, *49*, 11376−11378.

(27) Momma, K.; Izumi, F. VESTA 3 for Three-Dimensional Visualization of Crystal, Volumetric and Morphology Data. *J. Appl. Crystallogr.* **2011**, *44*, 1272−1276.

(28) Hung, I.; Zhou, L.; Pourpoint, F.; Grey, C. P.; Gan, Z. Isotropic High Field NMR Spectra of Li-Ion Battery Materials with Anisotropy>1 MHz. *J. Am. Chem. Soc.* **2012**, *134*, 1898−1901.

(29) Delmas, C.; Fouassier, C.; Hagenmuller, P. Structural Classification and Properties of the Layered Oxides. *Physica B+C* **1980**, *99*, 81−85.

(30) Fouassier, C.; Matejka, G.; Reau, J.-M.; Hagenmuller, P. Sur de nouveaux bronzes oxygénés de formule $Na_\chi CoO_2$ (χ<1). Le système cobalt-oxygène-sodium. *J. Solid State Chem.* **1973**, *6*, 532−537.

(31) Carlier, D.; Ménétrier, M.; Grey, C. P.; Delmas, C.; Ceder, G. Understanding the NMR Shifts in Paramagnetic Transition Metal Oxides Using Density Functional Theory Calculations. *Phys. Rev. B* **2003**, *67*, No. 174103.

(32) Ma, J.; Bo, S.-H.; Wu, L.; Zhu, Y.; Grey, C. P.; Khalifah, P. G. Ordered and Disordered Polymorphs of $Na(Ni_{2/3}Sb_{1/3})O_2$: Honeycomb-Ordered Cathodes for Na-Ion Batteries. *Chem. Mater.* **2015**, *27*, 2387−2399.

(33) Clément, R. J.; Bruce, P. G.; Grey, C. P. Review—Manganese-Based P2-Type Transition Metal Oxides as Sodium-Ion Battery Cathode Materials. *J. Electrochem. Soc.* **2015**, *162*, A2589−A2604.

(34) Zeng, D.; Cabana, J.; Bréger, J.; Yoon, W.-S.; Grey, C. P. Cation Ordering in $Li[Ni_xMn_xCo_{(1−2x)}]O_2$-Layered Cathode Materials: A Nuclear Magnetic Resonance (NMR), Pair Distribution Function, X-Ray Absorption Spectroscopy, and Electrochemical Study. *Chem. Mater.* **2007**, *19*, 6277−6289.

(35) Yoshida, J.; Guerin, E.; Arnault, M.; Constantin, C.; et al. New P2 - $Na_{0.70}Mn_{0.60}Ni_{0.30}Co_{0.10}O_2$ Layered Oxide as Electrode Material for Na-Ion Batteries. *J. Electrochem. Soc.* **2014**, *161*, A1987.

(36) Grundish, N. S.; Seymour, I. D.; Henkelman, G.; Goodenough, J. B. Electrochemical Properties of Three $Li_2Ni_2TeO_6$ Structural Polymorphs. *Chem. Mater.* **2019**, *31*, 9379−9388.

(37) Delmas, C.; Carlier, D.; Guignard, M. The Layered Oxides in Lithium and Sodium-Ion Batteries: A Solid-State Chemistry Approach. *Adv. Energy Mater.* 2001201. DOI: 10.1002/aenm.202001201.